Research Papers

GREENSUSMATER

Greensusmater
Vol. 3, No. 2, 2026, 13
https://doi.org/10.62755/gsm.2026.13

Check for updates

Influence of Molybdenum (Mo) Doping on the Morphology and Photocatalytic Activity of Hydrothermally Synthesized ZnO for Methylene Blue Degradation

Hirzi Alsyamadan[1], Muhammad Yasin Siregar[1], Mochammad Ghulam Isaq Khan[1,*]

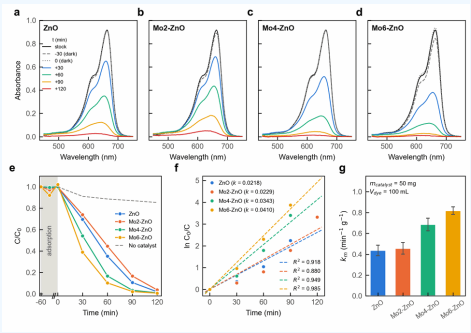
[1] *Department of Materials Engineering, Faculty of Industrial Technology, Institut Teknologi Sumatera, Terusan Ryacudu, Way Hui, Jati Agung, Lampung Selatan, 35365, Indonesia*

Corresponding author: mochammad.khan@mt.itera.ac.id

ARTICLE HISTORY: Received: September 30, 2026 | Revised: November 13, 2026 | Accepted: November 19, 2026

ABSTRACT

Zinc oxide (ZnO) is an inexpensive UV-active photocatalyst, but whether high-valent dopants such as Mo^{6+} enter its lattice during hydrothermal growth, and how they change its activity, remains poorly understood. Herein, molybdenum (Mo)-doped ZnO (2–6 mol% Mo) was synthesized via a urea-assisted hydrothermal route and calcination at 600 °C, and its lattice, morphology, optical absorption and activity were examined on the same samples. The samples were characterized by X-ray diffraction (XRD) with Rietveld refinement, scanning electron microscopy (SEM), Fourier-transform infrared (FTIR) spectroscopy and diffuse reflectance spectroscopy (DRS). All samples were single-phase wurtzite ZnO with crystallite sizes of 27–31 nm, and the lattice parameters varied by no more than 0.00015 Å in a and 0.0006 Å in c, indicating limited Mo substitution. However, Mo addition changed the particle morphology from porous nanoplatelet aggregates to dense prismatic particles up to hundreds of micrometers in size. The direct band gap decreased from 3.26 eV for pristine ZnO and Mo2-ZnO to 3.22 and 3.23 eV for Mo4-ZnO and Mo6-ZnO, while all samples absorbed the 254 nm excitation almost completely. Under UV-C irradiation, the apparent pseudo-first-order rate constant of methylene blue (MB) decolorization increased from $(21.8 \pm 2.5) \times 10^{-3}$ min^{-1} for pristine ZnO to $(41.0 \pm 1.8) \times 10^{-3}$ min^{-1} for Mo6-ZnO, whereas Mo2-ZnO performed like pristine ZnO. The activity gain thus coincided with the small band-gap decrease rather than with the lattice or the morphology, which suggests that Mo acts mainly through a small amount of surface species outside the bulk ZnO lattice.



Keywords: *Zinc Oxide; Molybdenum Doping; Hydrothermal Synthesis; Rietveld Refinement; Photocatalysis; Methylene Blue*

1. INTRODUCTION

Synthetic dyes released by the textile, paper and leather industries remain a persistent source of water pollution, because many of them resist biological treatment and stay colored at low concentrations [1,2]. Methylene blue (MB), a cationic thiazine dye, is widely used as a model pollutant because its strong absorption at 664 nm allows its removal to be followed directly by UV-Vis spectroscopy [3,4]. Adsorption can remove MB from water, but it transfers the dye to a solid phase that still requires disposal or regeneration [3].

Semiconductor photocatalysis offers an alternative in which photogenerated charge carriers produce reactive oxygen species that decompose the dye in situ [5,6]. Among the semiconductors studied for this purpose, including TiO_2, $BaTiO_3$, CeO_2 and g-C_3N_4, zinc oxide (ZnO) is attractive because it is inexpensive, non-toxic and active under UV irradiation [4,6,7]. However, the wide band gap of ZnO (about 3.3 eV) restricts its absorption to the UV region, and the fast recombination of photogenerated electrons and holes lowers its quantum efficiency [8,9].

Doping with metal cations is a common route to modify the electronic structure and defect chemistry of ZnO [8,10]. High-valent dopants such as Nb^{5+} have been introduced to create donor levels and to change the charge-carrier dynamics [9,11]. Molybdenum is a further candidate because it can adopt the +6 oxidation state, and Mo-doped ZnO has been prepared by several routes and tested against organic dyes [12–14]. In particular, Mo doping was reported to improve the photocatalytic degradation of rhodamine B over ZnO nanoparticles [15].

However, the large charge and size mismatch between Mo^{6+} (0.41 Å in four-fold coordination) and Zn^{2+} (0.60 Å) [16] raises the question of whether Mo enters the wurtzite lattice at all. In a previous study on Nb-doped ZnO prepared by a urea-assisted hydrothermal route, the lattice parameters changed only slightly and did not follow the Nb content, which pointed to limited substitution [17]. A dopant that remains outside the lattice may still influence the activity through the particle morphology or through surface species. Morphology is known to control the surface area and the active sites of photocatalysts [18]. For Mo in this hydrothermal route, the lattice response, the particle morphology and the photocatalytic activity have not been examined together on the same samples. It is therefore unclear which of these changes accompanies a change in activity.

The novelty of this work lies in testing, on one set of samples, whether the activity of Mo-doped ZnO follows a change of the lattice, of the morphology or of the optical absorption, rather than assuming substitutional doping from

© 2026 The Authors

This article is licensed under CC-BY 4.0 Open Access

the nominal composition. In this work, Mo-doped ZnO with nominal Mo/Zn molar ratios of 2, 4 and 6% was prepared by the same hydrothermal route used for Nb-doped ZnO [17] and compared with the pristine ZnO of that study. The crystal structure was analyzed by X-ray diffraction (XRD) with Rietveld refinement, the morphology by scanning electron microscopy (SEM), the surface species by Fourier-transform infrared (FTIR) spectroscopy, and the optical absorption by diffuse reflectance spectroscopy (DRS). The photocatalytic activity was evaluated through the decolorization of MB under UV-C irradiation, and the rate constants were compared with the run-to-run variation measured for the pristine ZnO powder. The kinetics are then related to the surface adsorption, charge-carrier and reactive-oxygen-species steps of the photocatalytic process, the performance is compared with previous Mo-doped ZnO studies, and a tentative mechanism is proposed.

2. MATERIALS AND METHODS

2.1 Materials

Zinc nitrate hexahydrate ($Zn(NO_3)_2{\cdot}6H_2O$, 98%, Sigma-Aldrich) was used as the zinc precursor. Urea ($CO(NH_2)_2$, Sigma-Aldrich) and polyvinylpyrrolidone (PVP, Sigma-Aldrich) served as the precipitating agent and surfactant, respectively [17]. Ammonium molybdate tetrahydrate (AMT, $(NH_4)_6Mo_7O_{24}{\cdot}4H_2O$, 99.98% trace metals basis, Sigma-Aldrich) was used as the Mo source. Methylene blue (MB, C.I. 52015, Merck, Darmstadt, Germany) was used as the model pollutant. All chemicals were used as received, and deionized water was used throughout.

2.2 Synthesis of Mo-Doped ZnO

Mo-doped ZnO was synthesized by a hydrothermal method with nominal Mo/Zn molar ratios of 2, 4 and 6%, following the procedure reported for Nb-doped ZnO [17]. For each sample, $Zn(NO_3)_2{\cdot}6H_2O$ (2.380 g, 8.0 mmol), urea (2.4 g) and PVP (5 wt% of the combined mass of $Zn(NO_3)_2{\cdot}6H_2O$ and AMT) were dissolved in 35 mL of deionized water and stirred for 20 min until homogeneous. AMT (0.028, 0.057 and 0.085 g for Mo/Zn ratios of 2, 4 and 6%, respectively) was dissolved separately in 35 mL of deionized water and stirred for 20 min. The Mo solution was then added slowly to the zinc solution under continuous stirring. The mixture was transferred into a Teflon-lined stainless-steel autoclave and heated at 175 °C for 24 h. The product was collected by vacuum filtration, dried at 80 °C for 6 h, calcined at 600 °C for 2 h with a heating rate of 3 °C min^{-1}, and ground in a mortar. The samples were designated Mo2-ZnO, Mo4-ZnO and Mo6-ZnO, respectively. Pristine ZnO prepared without dopant in the earlier study [17] served as the reference and is denoted ZnO.

2.3 Characterization

XRD patterns were recorded on a Rigaku SmartLab diffractometer in Bragg-Brentano geometry with Cu Kα radiation ($\lambda(K\alpha_1)$ = 1.540593 Å), a Kβ filter, a fixed 1/2° divergence slit, 2.5° Soller slits and a D/teX Ultra 250 detector. The patterns were collected from 5° to 80° 2θ with a step of 0.01° at 10° min^{-1}, and the four samples were measured consecutively in one session. Rietveld refinement [19] was performed over 20–80° 2θ with a wurtzite ZnO model (space group $P6_3mc$) in a Python implementation whose structure factors agreed with those of pymatgen to within 0.22 on a 100-point intensity scale. The peak profile was described by a Thompson-Cox-Hastings pseudo-Voigt function [20] with the Bérar-Baldinozzi asymmetry correction [21]. A Lorentzian term described the stacking-fault broadening of reflections with $h-k \neq 3n$ and $l \neq 0$ [22], and an order-4 spherical-harmonics function corrected the texture [23]. The scale factor, an eight-term Chebyshev background, the sample displacement, the lattice parameters, the profile parameters and the Cu Kβ leakage ratio were refined. The oxygen positional parameter was fixed at u = 0.382, close to the neutron-diffraction value [24]. The isotropic displacement parameters could not be refined stably with a 2θ limit of 80°. They were therefore fixed at B = 0.5 $Å^2$ (Zn) and 0.6 $Å^2$ (O), close to the values of 0.51 and 0.59 $Å^2$ obtained from single-crystal data at 293 K [25]. Anomalous dispersion corrections were taken from Henke et al. [26]. Repeating the refinement with four different parameter sets changed a by 0.00016–0.00028 Å, and this spread is used as a realistic uncertainty of the lattice parameters. The apparent crystallite size was estimated with the Scherrer equation (K = 0.9) [27] from the (100) and (002) reflections, which are not broadened by stacking faults. Their $K\alpha_1$ widths were obtained by fitting the 30.3–37.8° region with pseudo-Voigt $K\alpha_1/K\alpha_2$ doublets on a linear background. Instrumental and strain broadening were not subtracted, because no line-profile standard was measured, so the sizes are lower bounds.

The morphology was examined by SEM (JEOL JSM-6510) at 15 kV in secondary-electron mode after sputter coating with Pt. FTIR spectra were recorded in transmittance from 400 to 4000 cm^{-1} at a resolution of 8 cm^{-1} on a Thermo Scientific Nicolet iS10 spectrometer with a Smart iTR diamond ATR accessory. A spectrum of pristine ZnO from an independent batch prepared by the same route was recorded on a Shimadzu IRSpirit spectrometer in ATR mode and served as a Mo-free reference for band positions. Diffuse reflectance spectra of all four powders were recorded in one session from 190 to 800 nm on a Shimadzu UV-2600i Plus spectrophotometer with an integrating sphere. The reflectance R was converted with the Kubelka-Munk function, $F(R) = (1-R)^2/2R$. The direct band gap E_g was obtained by extrapolating the linear part of the plot of $(F(R)h\nu)^2$ against $h\nu$ to the energy axis [28]. The linear part was taken where the slope exceeded 70% of its maximum, and thresholds between 60% and 90% changed E_g by less than 0.01 eV.

2.4 Photocatalytic Tests

The photocatalytic activity was evaluated by the decolorization of MB under UV-C irradiation from four 10 W Philips TUV lamps ($\lambda \approx 254$ nm) [17]. In each test, 50 mg of catalyst was dispersed in 100 mL of MB solution (5 mg L^{-1}) prepared by diluting a 1000 mg L^{-1} stock. The suspension was stirred at 250 rpm in the dark for 60 min before the lamps were switched on. All tests were run at the natural, near-neutral pH of the MB solution in deionized water, without adjustment, at room temperature. Aliquots of 3.5 mL were withdrawn every 30 min, filtered, and their spectra were recorded from 200 to 800 nm on a Shimadzu UV-1280 spectrophotometer. The MB concentration was taken as proportional to the absorbance at 664 nm after subtracting the mean absorbance at 750–800 nm, where MB does not absorb, because the Beer-Lambert relation is linear for MB up to about 6 mg L^{-1}. The decolorization efficiency η was calculated from the absorbance values as η (%) = $(A_0 - A_t)/A_0 \times 100 = (C_0 - C_t)/C_0 \times 100$. Here A_0 and C_0 are the baseline-corrected absorbance at 664 nm and the concentration of the initial solution, and A_t and C_t are the corresponding values after a total time t. Dark adsorption was

© 2026 The Authors | CC-BY 4.0

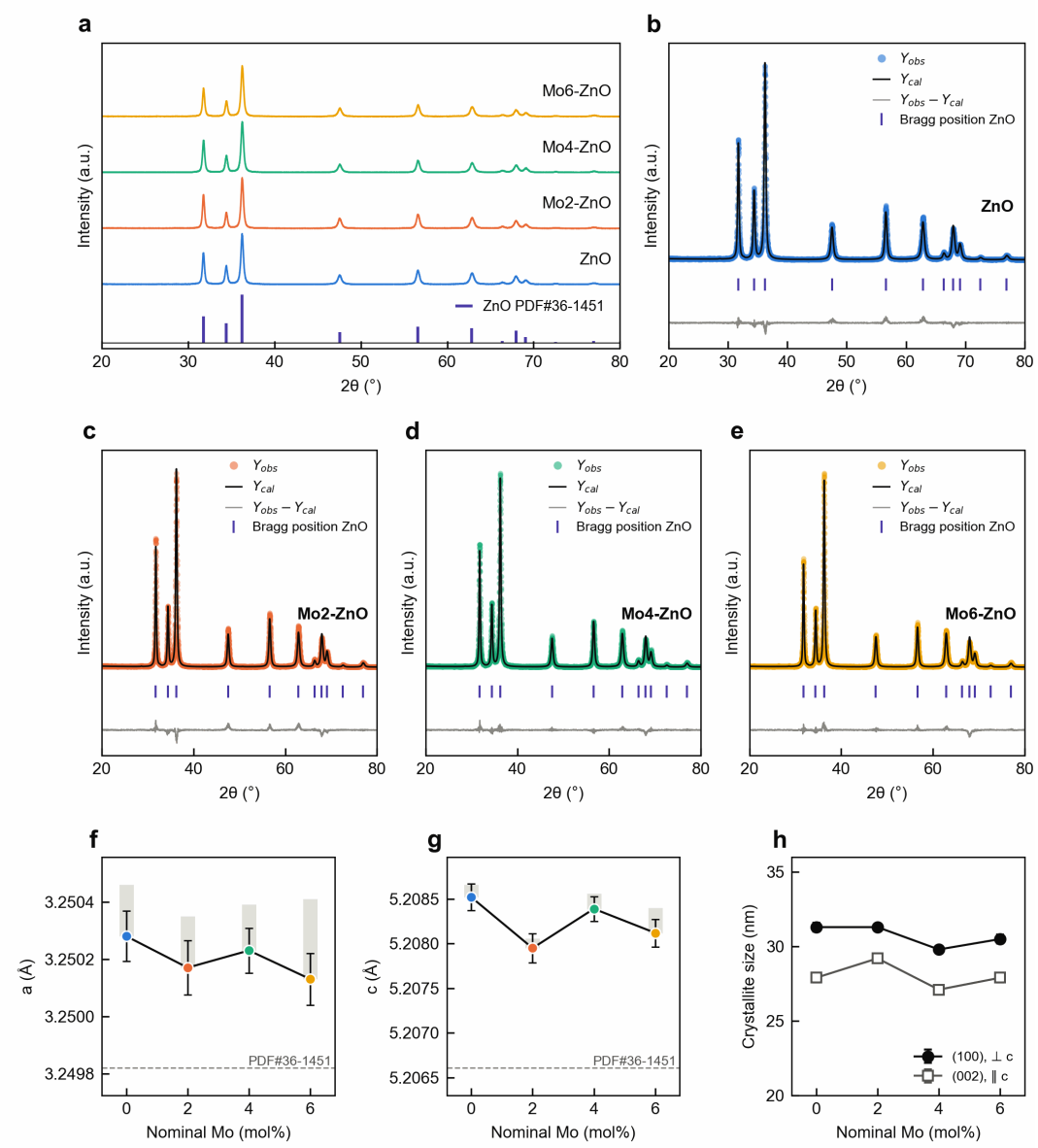


Figure 1. (a) XRD patterns of pristine ZnO and Mo-doped ZnO with the reference pattern of wurtzite ZnO (stick intensities calculated for the lattice parameters of ICDD PDF 00-036-1451). (b–e) Rietveld refinement plots of (b) pristine ZnO, (c) Mo2-ZnO, (d) Mo4-ZnO and (e) Mo6-ZnO. (f) Lattice parameter a and (g) lattice parameter c against nominal Mo content; error bars show statistical uncertainties, grey bars the range across refinement models, and dashed lines the ICDD values. (h) Apparent crystallite sizes from the (100) and (002) reflections.

obtained with the same expression from the absorbance at the end of the dark period. The decolorization was described by pseudo-first-order kinetics, $\ln(C_{on}/C) = k_{app}t$, where C_{on} is the concentration at the start of irradiation. The constant k_{app} was obtained by least-squares fitting through the origin, using the points with absorbance above the limit of quantification (0.018). The times to 50% and 90% decolorization (t_{50} and t_{90}) were obtained by log-linear interpolation. Direct photolysis was estimated from a catalyst-free MB control run in the same irradiation configuration in a separate session.

3. RESULTS AND DISCUSSION

3.1 Crystal Structure

The XRD patterns of pristine ZnO and the Mo-doped samples (Fig. 1a) show only the reflections of hexagonal wurtzite ZnO (ICDD PDF 00-036-1451, space group $P6_3mc$). No reflections of MoO_3 or $ZnMoO_4$ were detected above the noise level. Weak residual features near 28.4° and 30.8° 2θ and between 46° and 61° were traced to Cu Kβ leakage and to the Ni absorption edge of the filter. A further feature at about 26.5° (0.2% of the ZnO (101) intensity) appeared in both pristine ZnO and Mo6-ZnO and is therefore unrelated to Mo. The Rietveld refinements reproduced the patterns with R_{wp} values of 9.0–11.1% and χ^2 values of 1.34–2.18 (Fig. 1b–e and Table 1). The lattice parameters of the Mo-doped samples remain within 0.00015 Å (a) and 0.0006 Å (c) of those of pristine ZnO, and the cell volume changes by no more than 0.009 Å^3 (0.02%) (Table 1). These differences are comparable to the spread obtained when the refinement model was varied, so no systematic change with Mo content can be resolved (Fig.

© 2026 The Authors | CC-BY 4.0

Table 1. Lattice parameters and agreement indices from Rietveld refinement, and apparent crystallite sizes D_{100} and D_{002} from the Scherrer equation without instrumental correction. Statistical uncertainties in the last digit are given in parentheses.

Sample	a (Å)	c (Å)	c/a	V (Å^3)	D_{100} (nm)	D_{002} (nm)	R_{wp} (%)	R_{exp} (%)	χ^2	R_{Bragg} (%)
ZnO	3.25028(9)	5.20852(15)	1.60248(4)	47.653(3)	31.3(3)	27.9(3)	9.81	7.96	1.52	5.14
Mo2-ZnO	3.25017(9)	5.20795(16)	1.60236(5)	47.644(4)	31.3(2)	29.2(3)	11.14	7.54	2.18	7.37
Mo4-ZnO	3.25023(8)	5.20839(14)	1.60247(4)	47.650(3)	29.8(2)	27.1(3)	8.98	7.74	1.34	3.76
Mo6-ZnO	3.25013(9)	5.20812(16)	1.60243(5)	47.645(4)	30.5(3)	27.9(3)	10.30	7.75	1.77	4.89
PDF 00-036-1451	3.24982	5.20661	1.60213	47.62						

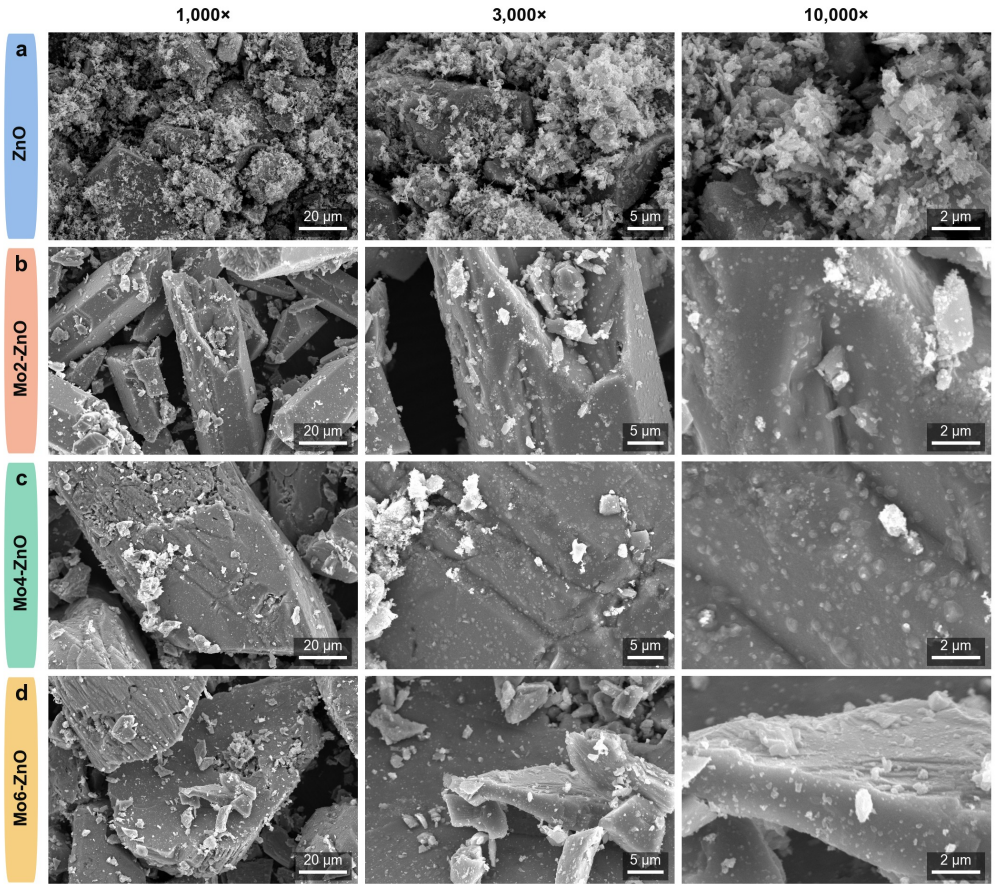


Figure 2. SEM images of (a) pristine ZnO, (b) Mo2-ZnO, (c) Mo4-ZnO and (d) Mo6-ZnO at 1,000×, 3,000× and 10,000× (left to right).

1f,g). Substitution of Zn^{2+} (0.60 Å) by the much smaller Mo^{6+} (0.41 Å) in tetrahedral sites [16] would be expected to contract the cell. A contraction growing with the Mo content would have been detectable if a large fraction of the nominal Mo had entered the lattice. The absence of such a trend therefore indicates that only a small fraction of Mo, if any, is incorporated substitutionally, consistent with the behavior of Nb in ZnO prepared by the same route [17]. All patterns show an hkl-dependent broadening in which reflections with $h-k \neq 3n$ and $l \neq 0$, such as (101), (102) and (103), are broader than (100), (002) and (110) at comparable angles. This pattern is characteristic of stacking faults in close-packed hexagonal structures [22], and the corresponding broadening parameters were of similar magnitude in all four samples. The Scherrer sizes obtained from the fault-free reflections were 29.8–31.3 nm for (100), perpendicular to the c axis, and 27.1–29.2 nm for (002), parallel to it (Fig. 1h and Table 1). Neither size followed the Mo content, so the crystallite-level microstructure of ZnO is not changed noticeably by Mo addition. The weak texture (texture index $J \leq 1.008$) is also similar for all samples. Because the lattice gives little evidence of Mo incorporation, the particle morphology and surface species were examined next.

3.2 Morphology, Surface Species and Optical Absorption

SEM images of pristine ZnO and the Mo-doped samples are compared in Fig. 2. Pristine ZnO consists mainly of porous aggregates of nanoplatelets and nanoparticles about 20–100 nm in size, with a few dense blocks beneath them (Fig. 2a). Mo2-ZnO consists of prismatic rods about 80–180 µm long and 20–30 µm wide (Fig. 2b). Mo4-ZnO and Mo6-ZnO consist of dense spindle-shaped or blocky particles up to about 250 µm long (Fig. 2c,d). These lengths were measured on images recorded at 100×, because the particles exceed the field of view at 1,000×. At 10,000× magnification, the faces of these particles are smooth and non-porous and carry scattered particles of 50–300 nm. Dense particles hundreds

© 2026 The Authors | CC-BY 4.0

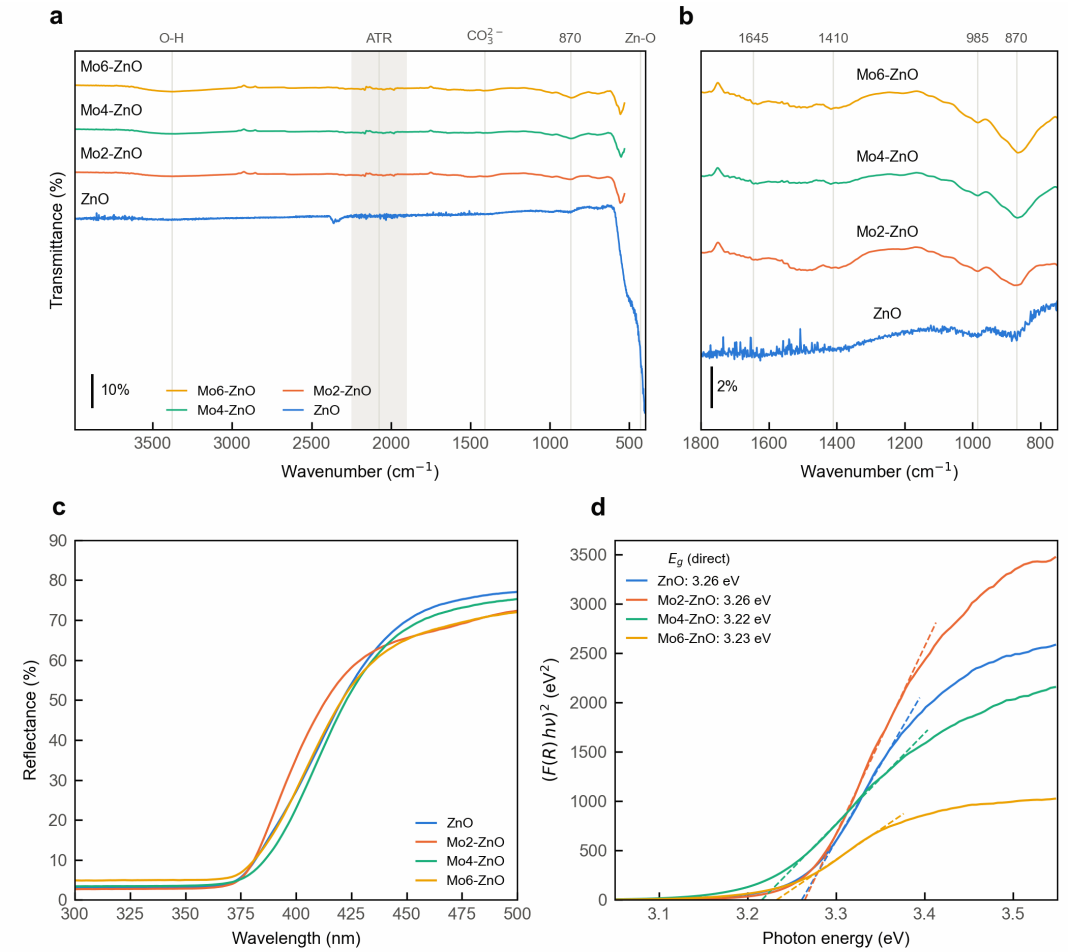


Figure 3. (a) FTIR transmittance spectra of pristine ZnO, Mo2-ZnO, Mo4-ZnO and Mo6-ZnO (offset for clarity), with the absorption region of the diamond ATR element shaded. (b) Enlarged 750–1800 cm^{-1} region. The pristine ZnO spectrum was recorded on an independent batch prepared by the same route, using a different instrument, and the spectra of the Mo-doped samples end at the 525 cm^{-1} cut-off. (c) Diffuse reflectance spectra in the 300–500 nm range. (d) Tauc plots of the Kubelka-Munk function for direct transitions with linear fits (dashed) and the resulting band gaps.

of micrometers in size combined with crystallites of about 30 nm, as in pristine ZnO (Section 3.1), indicate that these particles are polycrystalline aggregates rather than single crystals. The change therefore takes place at the level of particle growth and aggregation during the hydrothermal step. It may be related to molybdate species in the precursor solution, which could alter the precipitation and ripening of the zinc precursor phase. The pristine ZnO reference was imaged in a separate session, so part of the difference may also reflect batch-to-batch variation.

The FTIR transmittance spectra of pristine ZnO and the Mo-doped samples are compared in Fig. 3. Because the pristine ZnO spectrum was recorded on a different instrument, only band positions are compared. The Mo-doped samples show a broad O-H stretching band at 3377–3387 cm^{-1} and the H-O-H bending band of adsorbed water at 1645 cm^{-1}, and both bands are weak in pristine ZnO. Carbonate stretching bands appear between 1390 and 1490 cm^{-1} and may arise from adsorbed CO_2 or from residues of the urea precursor [29]. In pristine ZnO, the transmittance falls steeply below about 600 cm^{-1} and reaches 36% at 400 cm^{-1}, which corresponds to the Zn-O stretching band. For the Mo-doped samples, this band lies mostly below the 525 cm^{-1} limit of the measurement, and only its high-frequency shoulder is observed at 552–557 cm^{-1}. Two further bands at 866–868 and 985 cm^{-1} fall in the ranges of Mo-O-Mo and Mo=O stretching of molybdenum oxide species [30]. However, pristine ZnO shows bands at 870 and 986 cm^{-1} as well (Fig. 3b), so neither band can be attributed to Mo. The band at 866–870 cm^{-1} is therefore assigned to the out-of-plane bending mode of carbonate, consistent with the carbonate stretching bands. Its growth from Mo2-ZnO to Mo6-ZnO is matched by the O-H and water bands, which points to a difference in sample contact rather than in composition. The FTIR spectra therefore show no Mo-O vibration above the detection limit, in line with the absence of Mo phases in XRD. The diffuse reflectance spectra (Fig. 3c) show the absorption edge of ZnO between about 370 and 420 nm for all samples, and the reflectance at 254 nm is between 2.7% and 4.8%. All catalysts therefore absorb the UV-C excitation almost completely. The direct band gaps obtained from the Tauc plots (Fig. 3d) are 3.26 eV for pristine ZnO and Mo2-ZnO, and 3.22 and 3.23 eV for Mo4-ZnO and Mo6-ZnO, respectively. This decrease of 0.03–0.05 eV exceeds the fitting uncertainty, but a shift of this size can also arise from differences in particle size and packing of the powders, so it does not by itself indicate substitution of Mo.

© 2026 The Authors | CC-BY 4.0

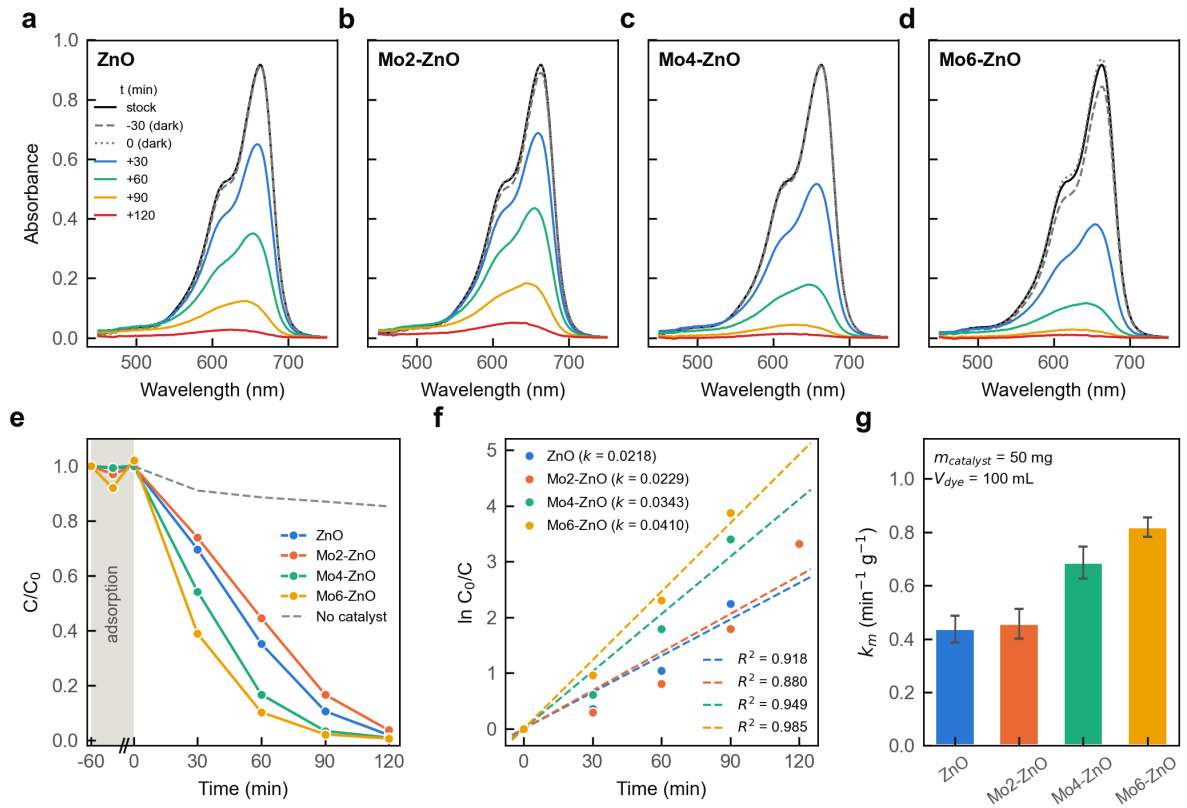


Figure 4. Photocatalytic decolorization of MB under UV-C irradiation. (a–d) UV-Vis spectra during the dark period and irradiation over (a) pristine ZnO, (b) Mo2-ZnO, (c) Mo4-ZnO and (d) Mo6-ZnO. (e) C/C_0 against time, including the catalyst-free control; the shaded area marks the dark adsorption period, shown on a compressed time axis. (f) Pseudo-first-order plots with fits through the origin. (g) Mass-normalized rate constants k_m with fit uncertainties.

The Mo-doped samples also reflect slightly less visible light, with 72.0–75.3% at 500 nm compared with 77.1% for pristine ZnO. This weak sub-gap absorption is largest for Mo2-ZnO and Mo6-ZnO and therefore does not follow the photocatalytic activity reported below. The photocatalytic behavior of the samples was evaluated next.

3.3 Photocatalytic Decolorization of MB

The evolution of the MB absorption spectra during the tests is shown in Fig. 4a–d, and the kinetic parameters are listed in Table 2. At the end of the 60 min dark period, the absorbance at 664 nm was within 2.2% of that of the initial solution for all catalysts (Fig. 4e). Adsorption therefore contributed negligibly to MB removal, and the subsequent decrease can be attributed to the irradiation. The catalyst-free control removed 14.7% of MB in 120 min (1.5×10^{-3} min^{-1}), which is small compared with the decolorization observed with the catalysts. Under irradiation, the MB band decreased steadily for all catalysts, and its maximum shifted from 663 nm to about 610–625 nm in the late stage (Fig. 4a–d). This hypsochromic shift is consistent with the stepwise N-demethylation of MB to azure and thionine intermediates [31], and MB is known to pass through several intermediates before mineralization [32]. The absorbance at 664 nm therefore measures decolorization rather than complete mineralization.

The plots of $\ln(C_{on}/C)$ against irradiation time (Fig. 4f) curve upwards, with negative intercepts of -0.16 to -0.38 when fitted freely, indicating a short induction period at the start of irradiation. The same curvature is present in an independent run of pristine ZnO [17], so it is a feature of the test configuration rather than of a particular sample. The rate constants fitted through the origin (Table 2 and Fig. 4f) are $(21.8 \pm 2.5) \times 10^{-3}$ min^{-1} for pristine ZnO and $(22.9 \pm 2.8) \times 10^{-3}$ min^{-1} for Mo2-ZnO. They rise to $(34.3 \pm 3.0) \times 10^{-3}$ min^{-1} for Mo4-ZnO and $(41.0 \pm 1.8) \times 10^{-3}$ min^{-1} for Mo6-ZnO. The model-free half-life times follow the same order, decreasing from 45 min for pristine ZnO to 32 min for Mo4-ZnO and 22 min for Mo6-ZnO, whereas Mo2-ZnO (53 min) did not differ from pristine ZnO. The mass-normalized constants (Fig. 4g) follow the same order.

The pseudo-first-order form of the kinetics can be related to the elementary steps of the photocatalytic process. In the Langmuir-Hinshelwood description, the rate is proportional to the fraction of surface sites occupied by MB. At the low concentration used here (5 mg L^{-1}, about 16 µM) this fraction is proportional to the concentration, which yields a first-order rate law. The negligible dark adsorption shows that MB is only weakly bound to the ZnO surface at the natural pH of the solution. The reaction is therefore not limited by the accumulation of dye on the catalyst but by the supply of reactive species at the surface. All catalysts absorb the 254 nm excitation to the same extent (Section 3.2). Conduction-band electrons then reduce dissolved O_2 to superoxide radicals ($\bullet O_2^-$), and valence-band holes oxidize surface hydroxide or water to hydroxyl radicals ($\bullet$OH) or oxidize adsorbed MB directly [6,33]. The steady-state concentration of these species,

© 2026 The Authors | CC-BY 4.0

Table 2. Photocatalytic decolorization of MB (5 mg L^{-1}, 50 mg catalyst in 100 mL, UV-C). Decolorization refers to 120 min of irradiation.

Sample	Dark adsorption (%)	Decolorization (%)	k_{app} (10^{-3} min^{-1})	R^2	k_m (min^{-1} g^{-1})	t_{50} (min)	t_{90} (min)
ZnO	0.3	98.1	21.8 ± 2.5	0.918	0.44	45	91
Mo2-ZnO	0.1	96.4	22.9 ± 2.8	0.880	0.46	53	100
Mo4-ZnO	−0.2	99.1	34.3 ± 3.0	0.949	0.69	32	70
Mo6-ZnO	−2.2	99.4	41.0 ± 1.8	0.985	0.82	22	60
ZnO, independent run [17]	12.5	91.7	18.3 ± 1.6	0.929		55	114
No catalyst		14.7	1.5				

and hence k_{app}, is set by the competition between charge separation and electron-hole recombination. The light absorbed, the crystal structure and the adsorption are the same for all samples. The higher k_{app} of Mo4-ZnO and Mo6-ZnO therefore indicates a larger steady-state yield of reactive species per absorbed photon, which points to slower recombination in these samples. The induction period in Fig. 4f is consistent with this picture. At the start of irradiation, part of the reactive species is consumed in forming the N-demethylated intermediates, which still absorb near 664 nm, before the absorbance at this wavelength falls at the full rate. A scavenger study is required to identify the dominant reactive species and was not part of this work. The effect of pH was not examined either, because the aim was to compare the four catalysts under one condition. Since the surface charge of ZnO and the adsorption of the cationic MB both depend on pH, this remains to be tested for the best sample.

The differences between the samples were assessed against the run-to-run variation of the reference catalyst. The MB data reported for the same pristine ZnO powder in the earlier study [17] were refitted with the procedure used here. This gave a rate constant of (18.3 ± 1.6) × 10^{-3} min^{-1}, 16% below the value measured in this work. The increases of 57% for Mo4-ZnO and 88% for Mo6-ZnO exceed this variation, whereas the 5% difference for Mo2-ZnO does not. Each Mo-doped catalyst was tested once, so the ranking of Mo4-ZnO in particular should be confirmed by replicate tests.

3.4 Relation Between Structure and Activity

Taken together, the results argue against three common explanations for the higher activity of Mo4-ZnO and Mo6-ZnO. First, the lattice parameters, the crystallite sizes and the stacking-fault broadening did not change with Mo content (Section 3.1), so the activity gain is not associated with a measurable change of the ZnO crystal structure. Second, the dense morphology is already present in Mo2-ZnO, which performs like pristine ZnO (Section 3.2), so the morphology change alone does not explain the activity. The larger particles would also be expected to reduce rather than increase the accessible surface area [18]. Third, all catalysts absorbed the 254 nm excitation almost completely (Section 3.2), so the amount of light absorbed under UV-C was essentially the same. Neither XRD nor FTIR detected a separate Mo phase, so any Mo retained in the solids is present in small amounts or in a poorly crystalline, dispersed form. Such Mo species at the surface or at grain boundaries of ZnO could accept photogenerated electrons and reduce electron-hole recombination without changing the lattice. A tentative pathway consistent with these observations is as follows. Under 254 nm irradiation, ZnO generates electron-hole pairs across its band gap of 3.22–3.26 eV. The conduction-band edge of ZnO (about −0.3 V vs. NHE) lies above the $O_2/{\bullet}O_2^-$ potential (−0.33 V), and the valence-band edge (about +2.9 V) lies well below the $OH^-/{\bullet}OH$ potential (+1.99 V) [33,34]. Both superoxide and hydroxyl radicals can therefore form, and holes can also oxidize adsorbed MB directly. These species attack the methyl groups and the thiazine ring of MB. This gives the N-demethylated intermediates observed as the hypsochromic shift in Fig. 4a–d and, on longer irradiation, smaller fragments [31,32]. Mo^{6+} centers in dispersed molybdate species at the surface could be reduced transiently to Mo^{5+} by conduction-band electrons and pass them on to O_2. This would delay recombination and leave more holes for oxidation. The slightly lower band gaps of Mo4-ZnO and Mo6-ZnO, which follow the activity order, would be consistent with such Mo-related states near the band edges, but the shift is too small to be conclusive. The present data do not include a direct measurement of the Mo content or distribution in the solids, which is the main limitation of this work. This interpretation therefore remains to be tested by EDS elemental mapping and XPS of the Mo 3d region, which would establish the amount, distribution and oxidation state of the retained Mo. Measurements of the specific surface area and the photoluminescence are also required.

The present results can be placed against previous reports, although the dye, its concentration, the catalyst dose, the light source and the kinetic treatment differ between studies, so the values are not directly comparable. Under UV-C irradiation of 5 mg L^{-1} MB at 0.5 g L^{-1} catalyst, Mo6-ZnO removed 99.4% of MB in 120 min with a rate constant of 41.0 × 10^{-3} min^{-1}, 1.9 times that of the same pristine ZnO powder (98.1%, 21.8 × 10^{-3} min^{-1}). Nb-doped ZnO prepared by the same route and tested in the same set-up gave no gain for MB, with 90.7% removal and 19.9 × 10^{-3} min^{-1} for Nb4-ZnO against 91.7% and 21.0 × 10^{-3} min^{-1} for pristine ZnO [17]. A twofold gain of similar size was reported for 5 wt% Mo-doped ZnO prepared by reflux against 10 mg L^{-1} rose bengal under UV light, with 91% removal in 30 min and rate constants of 131 and 62 × 10^{-3} min^{-1} for the doped and undoped catalysts [14]. Hydrothermal Mo-ZnO nanoflowers with 1% Mo removed 97% of 10 mg L^{-1} MB in 40 min under sunlight against 77% for undoped ZnO [35]. The present study differs from these Mo-ZnO reports in that the gain is obtained without evidence of lattice substitution, which those studies inferred from the nominal composition or from small peak shifts.

4. CONCLUSIONS

Mo-doped ZnO with nominal Mo/Zn molar ratios of 2, 4 and 6% was prepared by a urea-assisted hydrothermal route and compared with pristine ZnO for the photocatalytic decolorization of MB under UV-C irradiation. Rietveld refinement showed single-phase wurtzite ZnO in all samples, with lattice parameters that did not change with Mo content beyond the model uncertainty, indicating that only a small fraction

© 2026 The Authors | CC-BY 4.0

of Mo, if any, entered the ZnO lattice. The crystallite sizes of 27–31 nm and the stacking-fault broadening were also unchanged. However, Mo addition changed the particle morphology from porous nanoplatelet aggregates to dense prismatic and spindle-shaped particles. The FTIR bands near 870 and 986 cm^{-1} were also present in pristine ZnO, so no evidence of Mo-O vibrations was found. The direct band gap decreased slightly, from 3.26 eV for pristine ZnO and Mo2-ZnO to 3.22 and 3.23 eV for Mo4-ZnO and Mo6-ZnO, while all samples absorbed the 254 nm excitation almost completely. Among the samples investigated, Mo6-ZnO gave the highest rate constant, $(41.0 \pm 1.8) \times 10^{-3}$ min^{-1}, 88% above that of pristine ZnO, followed by Mo4-ZnO, whereas Mo2-ZnO performed like pristine ZnO. The activity gain thus followed the small band-gap decrease, but not the lattice or the morphology. It may originate from small amounts of Mo retained at the surface or grain boundaries of ZnO, which could introduce states near the band edges and reduce electron-hole recombination, increasing the yield of superoxide and hydroxyl radicals that N-demethylate and fragment MB. The rate constant of Mo6-ZnO is about twice that of pristine ZnO and of Nb-doped ZnO prepared by the same route, a gain comparable to earlier Mo-ZnO reports under UV light. Future work should focus on replicate photocatalytic tests, scavenger tests and the effect of pH, quantification of the Mo content and oxidation state by EDS mapping and XPS, and measurements of the surface area and photoluminescence to establish the mechanism.

AUTHOR CONTRIBUTIONS

Hirzi Alsyamadan: Investigation, Data curation, Visualization. Muhammad Yasin Siregar: Methodology, Validation, Writing – Review & Editing. Mochammad Ghulam Isaq Khan: Conceptualization, Methodology, Formal analysis, Validation, Writing – Original Draft, Writing – Review & Editing, Supervision.

CONFLICT OF INTEREST

The authors declare that they have no known competing financial interests or personal relationships that could have appeared to influence the work reported in this paper.

USE OF AI-ASSISTED TECHNOLOGIES

During the preparation of this work, the authors used Claude (Anthropic) to assist with drafting of the text. After using this tool, the authors reviewed and edited the content as needed and take full responsibility for the content of the publication.

DATA AVAILABILITY

Data will be made available on request.

FUNDING

This research did not receive any specific grant from funding agencies in the public, commercial, or not-for-profit sectors.

REFERENCES

[1] Chen Z, Wei W, Chen H, Ni BJ. Recent advances in waste-derived functional materials for wastewater remediation. *Eco-Environ. Health*. 2022;1:86-104. doi:10.1016/j.eehl.2022.05.001.

[2] Habibollahi Z, Peyravi M, Khalili S, Jahanshahi M. ZnO-based ternary nanocomposite for decolorization of methylene blue by photocatalytic dynamic membrane. *Mater. Today Chem.* 2022;23:100748. doi:10.1016/j.mtchem.2021.100748.

[3] Fitri A, Prasetya B, Aini Q, Ikhsan F, Aflaha R, Triyana K, Taher T, Arif MF, Rianjanu A. Enhanced methylene blue adsorption capacity of 3D-printed zeolite/glycerol (3D-Ze/Gy) by sintering temperature optimalizations. *Next Mater.* 2025;9:101069. doi:10.1016/j.nxmate.2025.101069.

[4] Pantoja-Espinoza JC, DelaCruz-Alderete GA, Paraguay-Delgado F. Photocatalytic degradation of methylene blue dye with g-C_3N_4/ZnO nanocomposite materials using visible light. *Catalysts*. 2025;15:851. doi:10.3390/catal15090851.

[5] Rianjanu A, Aini Q, Hanif R, Tambun SA, Triyadi D, Aflaha R, Yulianto N, Yudistira HT, Herbani Y, Taher T, Wasisto HS. Influence of temperature and reaction time on photocatalytic performance of $BaTiO_3$ nanoparticles for organic pollutant degradation in aqueous environment. *Surf. Interfaces*. 2025;70:106875. doi:10.1016/j.surfin.2025.106875.

[6] Khan MGI, Nurfitria R, Anggraini T, Aini Q, Hanifah IR, Nurfani E, Aflaha R, Triyana K, Taher T, Rianjanu A. Hydrothermal synthesis of CeO_2/ZnO heterojunctions for effective photocatalytic degradation of organic pollutants. *Mater. Sci. Eng. B*. 2025;322:118630. doi:10.1016/j.mseb.2025.118630.

[7] Phasa A, Aini Q, Siregar MY, Sabilla S, Triyadi D, Aflaha R, Khan MGI, Nurfani E. Photocatalytic degradations of organic pollutants in wastewater using hydrothermally grown ZnO nanoparticles. *Greensusmater*. 2024;1:39-43. doi:10.62755/greensusmater.2024.1.2.39-43.

[8] Qi K, Xing X, Zada A, Li M, Wang Q, Liu SY, Lin H, Wang G. Transition metal doped ZnO nanoparticles with enhanced photocatalytic and antibacterial performances: experimental and DFT studies. *Ceram. Int.* 2020;46:1494-1502. doi:10.1016/j.ceramint.2019.09.116.

[9] Silva JMP, Julião RS, Nicácio TCN, Melo MCN, Santos RM, Bomio MRD, Motta FV. A study of Nb-doped ZnO ceramic and its enhanced solar photocatalysis, photoluminescence and antimicrobial properties. *J. Alloys Compd.* 2024;985:173978. doi:10.1016/j.jallcom.2024.173978.

[10] Ameen S, Fatima R, Kadhem AA, Abbas T, Khan MA, Abbas A, Hussain I, Bano N, Faraji Rad Z, Bilal ASS. Enhanced photocatalytic degradation of methylene blue using aluminum and cerium co-doped ZnO nanocomposite. *Int. J. Environ. Sci. Technol.* 2025;22:16549-16558. doi:10.1007/s13762-025-06683-z.

[11] Nguyen THA, Le VT, Doan VD, Tran AV, Nguyen VC, Nguyen AT, Vasseghian Y. Green synthesis of Nb-doped ZnO nanocomposite for photocatalytic degradation of tetracycline antibiotic under visible light. *Mater. Lett.* 2022;308:131129. doi:10.1016/j.matlet.2021.131129.

[12] Yu C, Yang K, Shu Q, Yu JC, Cao F, Li X, Zhou X. Preparation, characterization and photocatalytic performance of Mo-doped ZnO photocatalysts. *Sci. China Chem.* 2012;55:1802-1810. doi:10.1007/s11426-012-4721-8.

[13] Khalid NR, Sabir M, Ali F, Tahir MB, Javid MA, Niaz NA, Ahmed R, Rafique M, Imran M, Assiri MA. Green synthesis and characterizations of bi-functional Mo-doped ZnO nanostructures for antimicrobial and photocatalytic applications. *Mater. Chem. Phys.* 2023;296:127306. doi:10.1016/j.matchemphys.2023.127306.

[14] Kadam V, Jagtap C, Kumkale V, Rednam U, Lokhande P, Pathan H. Photocatalytic degradation of rose bengal dye using chemically synthesized pristine and molybdenum doped zinc oxide. *Eng. Sci.* 2024;28:1077. doi:10.30919/es1077.

[15] Kohzadi S, Maleki A, Bundschuh M, Vahabzadeh Z, Johari SA, Rezaee R, Shahmoradi B, Marzban N, Amini N. Doping zinc oxide (ZnO) nanoparticles with molybdenum boosts photocatalytic degradation of Rhodamine b (RhB): particle characterization, degradation kinetics and aquatic toxicity testing. *J. Mol. Liq.* 2023;385:122412. doi:10.1016/j.molliq.2023.122412.

[16] Shannon RD. Revised effective ionic radii and systematic studies of interatomic distances in halides and chalcogenides. *Acta Crystallogr. A*. 1976;32:751-767. doi:10.1107/S0567739476001551.

[17] Aini Q, Putri CIS, Nurfitria R, Hanifah IR. Influence of Nb dopant concentration on the structural properties and photocatalytic performances of hydrothermally synthesized

© 2026 The Authors | CC-BY 4.0

ZnO for multi-pollutant degradation. *Greensusmater*. 2026;3:01. doi:10.62755/gsm.2026.01.

[18] Ganguli AK, Kunde GB, Raza W, Kumar S, Yadav P. Assessment of performance of photocatalytic nanostructured materials with varied morphology based on reaction conditions. *Molecules*. 2022;27:7778. doi:10.3390/molecules27227778.

[19] Rietveld HM. A profile refinement method for nuclear and magnetic structures. *J. Appl. Crystallogr.* 1969;2:65-71. doi:10.1107/S0021889869006558.

[20] Thompson P, Cox DE, Hastings JB. Rietveld refinement of Debye-Scherrer synchrotron X-ray data from Al_2O_3. *J. Appl. Crystallogr.* 1987;20:79-83. doi:10.1107/S0021889887087090.

[21] Bérar JF, Baldinozzi G. Modeling of line-shape asymmetry in powder diffraction. *J. Appl. Crystallogr.* 1993;26:128-129. doi:10.1107/S0021889892009725.

[22] Warren BE. *X-ray Diffraction*. 1969.

[23] Järvinen M. Application of symmetrized harmonics expansion to correction of the preferred orientation effect. *J. Appl. Crystallogr.* 1993;26:525-531. doi:10.1107/S0021889893001219.

[24] Kisi EH, Elcombe MM. u parameters for the wurtzite structure of ZnS and ZnO using powder neutron diffraction. *Acta Crystallogr. C*. 1989;45:1867-1870. doi:10.1107/S0108270189004269.

[25] Sowa H, Ahsbahs H. High-pressure X-ray investigation of zincite ZnO single crystals using diamond anvils with an improved shape. *J. Appl. Crystallogr.* 2006;39:169-175. doi:10.1107/S0021889805042457.

[26] Henke BL, Gullikson EM, Davis JC. X-ray interactions: photoabsorption, scattering, transmission, and reflection at E = 50-30,000 eV, Z = 1-92. *At. Data Nucl. Data Tables*. 1993;54:181-342. doi:10.1006/adnd.1993.1013.

[27] Patterson AL. The Scherrer formula for X-ray particle size determination. *Phys. Rev.* 1939;56:978-982. doi:10.1103/PhysRev.56.978.

[28] Makuła P, Pacia M, Macyk W. How to correctly determine the band gap energy of modified semiconductor photocatalysts based on UV-Vis spectra. *J. Phys. Chem. Lett.* 2018;9:6814-6817. doi:10.1021/acs.jpclett.8b02892.

[29] Busca G, Lorenzelli V. Infrared spectroscopic identification of species arising from reactive adsorption of carbon oxides on metal oxide surfaces. *Mater. Chem.* 1982;7:89-126. doi:10.1016/0390-6035(82)90059-1.

[30] Seguin L, Figlarz M, Cavagnat R, Lassègues JC. Infrared and Raman spectra of MoO_3 molybdenum trioxides and $MoO_3 \cdot xH_2O$ molybdenum trioxide hydrates. *Spectrochim. Acta A*. 1995;51:1323-1344. doi:10.1016/0584-8539(94)00247-9.

[31] Zhang T, Oyama T, Aoshima A, Hidaka H, Zhao J, Serpone N. Photooxidative N-demethylation of methylene blue in aqueous TiO_2 dispersions under UV irradiation. *J. Photochem. Photobiol. A*. 2001;140:163-172. doi:10.1016/S1010-6030(01)00398-7.

[32] Houas A, Lachheb H, Ksibi M, Elaloui E, Guillard C, Herrmann JM. Photocatalytic degradation pathway of methylene blue in water. *Appl. Catal. B*. 2001;31:145-157. doi:10.1016/S0926-3373(00)00276-9.

[33] Nosaka Y, Nosaka AY. Generation and detection of reactive oxygen species in photocatalysis. *Chem. Rev.* 2017;117:11302-11336. doi:10.1021/acs.chemrev.7b00161.

[34] Xu Y, Schoonen MAA. The absolute energy positions of conduction and valence bands of selected semiconducting minerals. *Am. Mineral.* 2000;85:543-556. doi:10.2138/am-2000-0416.

[35] Padwal Y, Chauhan R, Panchang R, Fouad H, Gosavi SW. Exploring Mo-ZnO@NF for hydrogen generation and methylene blue remediation: sunlight-driven catalysis. *Front. Phys.* 2024;12:1416563. doi:10.3389/fphy.2024.1416563.

© 2026 The Authors | CC-BY 4.0